



An investigation of LnUO₄ (Ln = Dy and Ho): Structures, microstructures, uranium valences and magnetic properties

Kimbal T. Lu^{a,b}, Yingjie Zhang^{a,*}, Tao Wei^a, Zhaoming Zhang^a, Maxim Avdeev^a, Rongkun Zheng^b

^a Australian Nuclear Science and Technology Organisation, Locked Bag 2001, Kirrawee DC, New South Wales, 2232, Australia

^b School of Physics, The University of Sydney, Camperdown, New South Wales, 2006, Australia

ARTICLE INFO

Keywords:

Dysprosium
Holmium
Uranium
Monouranate
Magnetism

ABSTRACT

The phase formation, structures, microstructures, uranium valences and magnetic properties of LnUO₄ (Ln = Dy and Ho) were investigated. Although sintering of the precursors in argon at 1450 °C for seven days and 1400 °C for six hours both resulted in the desired phase, sintering at higher temperature for longer duration led to the formations of well crystallized lanthanide monouranates with much better homogeneity. Cubic fluorite structures were determined using X-ray diffraction data, which was confirmed with transmission electron microscopy and Raman spectroscopy. The nature of pentavalent uranium was verified with a combination of diffuse reflectance and X-ray photoelectron spectroscopies. The magnetic susceptibility measurements revealed that they are paramagnetic with no long-range magnetic orders, likely due to the extensive short-range oxygen defects. Overall the improved structural and spectroscopic understandings of LnUO₄ have implications in nuclear materials especially for potential accident tolerance fuels and spent fuel management.

1. Introduction

Metal monouranates in the form of MUO₄ have attracted a growing interest due to their importance in uranium crystal chemistry and implications in nuclear industry, *e.g.*, their close relationships to UO₂ based nuclear fuels such as accident tolerance fuels and the potential role in the management of spent nuclear fuels [1–3]. From the crystal-chemical point of view, hexavalent uranium species in the form of uranyl (UO₂²⁺) ion, including many uranyl minerals [7–9], dominate uranium aqueous and crystal chemistry [4–6] in regards to environmental and geological aspects, largely due to its greater solubility and mobility in the environment, in comparison to much less soluble U⁴⁺ species present in UO₂ and its associated compounds. However, the intermediate pentavalent oxidation state of uranium, U⁵⁺, which can often be found in aqueous solutions [10,11] and is anticipated to be present in some metal monouranates, is less common and has not been well studied [12,13]. Although observed in aqueous solutions under particular redox conditions, U⁵⁺ present in the UO₂⁺ molecular ion is strongly subjected to disproportionation, which reduces drastically its life-time in these media, compared to U⁴⁺ in reducing and U⁶⁺ in oxidative conditions. While MUO₄ with divalent cations M²⁺ (M = Mg, Ca, Sr, Ba, Ni, Co, Mn

and Cd) [14–20] require the oxidation state of U to be hexavalent U⁶⁺ for charge balance, the pentavalent U⁵⁺ ions could possibly be stabilized in MUO₄ with the presence of trivalent metal ions, *e.g.*, M³⁺ = Cr, Fe, Bi, Sc and Y [19–25], yet the exact U valences are less certain in many of those cases.

It is understood that cubic-structured phases are dominating in the system UO₂–(Y/Ln)₂O₃ for the entire compositional range [26–33]. The observed non-linear variation of the lattice parameters was initially explained based on the fact that the substitution increases the amount of anionic vacancies with increasing (Y/Ln)₂O₃ content in UO₂, assuming that uranium remains in tetravalent oxidation state. In addition, the charge compensation mechanisms and U valences with Nd/Gd doped UO₂ have been extensively studied [34–36]. More recently, a comprehensive study on the oxidation states of U in the Bi–U–O system confirmed that BiUO₄ is a pure pentavalent uranium phase [23]. It is anticipated that the formation of pentavalent U in UO₂–(Y/Ln)₂O₃ system could account for the non-linear variation of the lattice parameters upon (Y/Ln)₂O₃ incorporations in UO₂. With equal molar of Ln and U, LnUO₄ can be formed by sintering in neutral and slightly reducing atmospheres [26–33]. Since the magnetic susceptibility measurements for BiUO₄, ScUO₄ and YUO₄ confirmed that they are metal monouranates

* Corresponding author.

E-mail address: yzx@ansto.gov.au (Y. Zhang).

<https://doi.org/10.1016/j.jeurceramsoc.2021.05.040>

Received 19 February 2021; Received in revised form 13 May 2021; Accepted 19 May 2021

Available online 21 May 2021

0955-2219/Crown Copyright © 2021 Published by Elsevier Ltd. All rights reserved.

with pure pentavalent uranium [24,25], showing the same maximum at 4–7 K with a similar shape in the magnetic susceptibility vs. temperature curves, it was reasonable to assume that LnUO_4 might also contain pure pentavalent uranium based on the linear trend of lattice parameters against ionic radius [23]. If the presence of pentavalent U^{5+} ions is proven in lanthanide monouranates, LnUO_4 phases with cubic structures and simple stoichiometry would allow some in-depth structural and spectroscopic studies to improve our fundamental understandings on these mixed lanthanide and uranium oxides.

Despite the increasing attention to LnUO_4 compounds and their importance in the uranium based nuclear fuel cycle, only a few structural characterizations are currently available [26–36] and very limited spectroscopic measurements have been used to probe the local structures [23,34–36]. The primary aim of the current work was to gain a better understanding of LnUO_4 materials in regards to their crystal chemistry and properties, in specific the phase formation, structures and microstructures, uranium valences and magnetic properties of LnUO_4 ($\text{Ln} = \text{Dy}$ and Ho). Both Dy and Ho were used as neutron poisons in the nuclear fuels due to their relatively large cross sections for neutrons. As such their incorporations in UO_2 and phase stabilization deserve further research effort. In addition, DyUO_4 was not reported before. Consequently, Dy and Ho were chosen for this study.

2. Experimental

2.1. Sample preparation

Both DyUO_4 and HoUO_4 precursors were prepared by mixing equal molar of uranyl nitrate hexahydrate and dysprosium/holmium nitrate hexahydrate (from Sigma-Aldrich) in deionized water, drying in an oven at 110 °C followed by calcining at 750 °C in argon for 6 h. The precursors were pelletized (~1 g) and then sintered in argon at 1400 °C for 6 h (DyUO_4) and 1450 °C for 7 days (DyUO_4 and HoUO_4). The sintering conditions were chosen largely based on the available literature. A preliminary TGA of the DyUO_4 precursor showed a gradual weight loss from 1000 to 1200 °C, indicating that the reduction of U^{6+} to U^{5+} requires higher sintering temperature. In addition, the observed inhomogeneity in the initial DyUO_4 sample sintered at 1400 °C for 6 h could be due to both the thermodynamic (temperature) and kinetic (holding time) factors. Subsequently, higher sintering temperature (1450 °C) and longer holding time (7 days) were chosen to address this in order to achieve the satisfactory results.

2.2. X-ray diffraction

The X-ray diffraction (XRD) data were collected on a Bruker D8 Focus diffractometer equipped with $\text{Cu-K}\alpha$ ($\lambda = 1.5418 \text{ \AA}$) radiation, in the range $10^\circ < 2\theta < 120^\circ$, with a step size of 0.02° (2θ) and an acquisition time of 4 s per step. Unit cell parameters were determined with the Le Bail method [37] using the RIETICA program (version 2.1) [38]. The peak profiles were approximated by the Pseudo-Voigt function, and the background was estimated by a 6 term polynomial function. The lattice parameters were refined together with the peak profile parameters until the R factors ceased to change.

2.3. Scanning electron microscopy

Scanning electron microscopy (SEM) was used to analyze the morphology and energy dispersive spectroscopy (EDS) to determine the Ln to U ratios. Samples were mounted in resin, carbon coated and examined in a Zeiss Ultra Plus scanning electron microscope (Carl Zeiss NTS GmbH, Oberkochen, Germany) operating at 15 kV equipped with an Oxford Instruments X-Max 80 mm^2 SDD X-ray microanalysis system. The finely crushed samples were dusted onto conducting carbon sticky tapes and then carbon coated before SEM analysis. The sintered samples were mounted in resin, polished to 1 μm finish using a diamond paste

and then carbon coated for SEM analysis. The EDS multiple point analyses were carried out on polished sample surfaces with Cu standard for calibration.

2.4. Transmission electron microscopy

Transmission electron microscopy (TEM) experiments were carried out using a JEOL 2200FS (JEOL Ltd, Japan) operated at 200 keV, fitted with an Oxford X-Max silicon drift detector for Energy Dispersive X-ray Spectroscopy. TEM specimens consist of crushed grains dispersed in ethanol and then dispensed onto a holey carbon film supported on a TEM copper mesh grid.

2.5. Diffuse reflectance spectroscopy

Diffuse reflectance spectra (DRS) in both UV–vis and NIR regions were recorded on an Agilent Cary 5000 spectrophotometer equipped with a Labsphere Biconical Accessory.

2.6. Raman spectroscopy

Raman spectra were collected on a Renishaw inVia spectrometer equipped with a 785 nm excitation Ar laser with a spectral resolution of $\sim 1.7 \text{ cm}^{-1}$. The spectrometer was calibrated by measuring a monocrystalline Si with the T_{2g} band set at 520.5 cm^{-1} . The laser beam was focused on the sample through a long focal distance (1 cm) objective (Numerical Aperture = 0.5) with 50x magnification. The laser spot size on the sample was $\sim 1.5 \mu\text{m}^2$. The excitation power (5 mW) was optimized to prevent possible sample oxidation and damage.

2.7. X-ray photoelectron spectroscopy (XPS)

The HoUO_4 sample was examined in ultra-high vacuum with a Thermo Scientific ESCALAB 250Xi XPS system employing a monochromatic Al $\text{K}\alpha$ (1486.6 eV) X-ray source. The X-ray gun was operated at 120 W, and the spectrometer pass energy was set at 20 eV for regional scans. The diameter of the analysis area was approximately 500 μm . The thickness of the probed surface layer was approximately 5 nm. A low energy electron flood gun was used for the neutralization of surface charge build up due to low electrical conductivity of the HoUO_4 sample. The binding energies were calibrated by fixing the C 1s peak (due to adventitious carbon) at 285.0 eV. Peak fitting of the U $4f_{7/2}$ region, after the subtraction of a Shirley-type background, was performed using the CasaXPS software package [39].

2.8. Magnetic susceptibility

Magnetic susceptibility data were collected using a PPMS9 magnetometer (Quantum Design) calibrated against a standard palladium sample. Zero-field cooled (ZFC) and field cooled (FC) DC susceptibility was measured under the field of 1000 Oe in the temperature range of 2.5–300 K. The data were corrected for diamagnetism using the Pascal's constants.

3. Results and discussion

3.1. Phase formation and structures

Earlier works [26–33] had established that lanthanide oxides can form solid solutions with UO_2 in cubic fluorite structures. With equal molar of Ln and U, LnUO_4 phases can be formed by sintering under either neutral or reducing atmospheres. In this work, the DyUO_4 pellets were sintered in argon at either 1400 °C for 6 h or 1450 °C for 7 days and the HoUO_4 pellet was sintered in argon at 1450 °C for 7 days to investigate the phase formation and structures. The XRD patterns (Fig. 1) revealed that cubic structured DyUO_4 and HoUO_4 were formed by

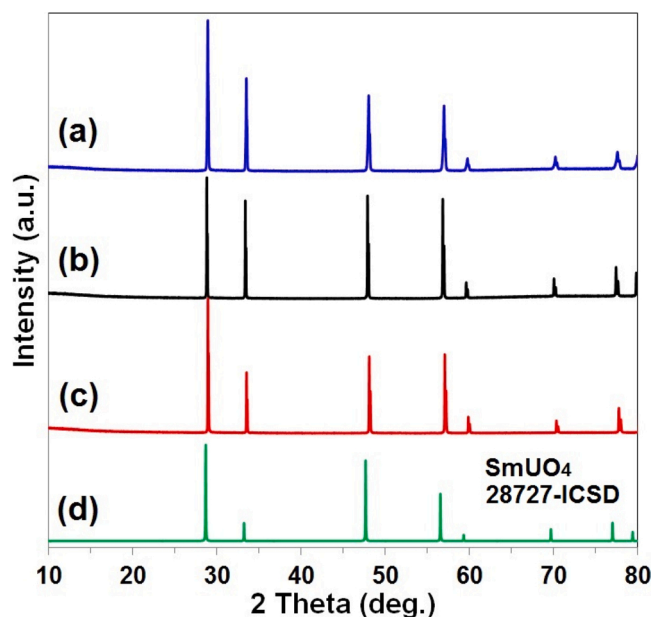


Fig. 1. XRD patterns of sample Dy_2UO_7 sintered in argon at either 1400 °C for 6 h (a), or at 1450 °C for 7 days (b) and sample Ho_2UO_7 sintered in argon at 1450 °C for 7 days (c), together with that of Sm_2UO_7 (d) as a reference.

sintering at either 1400 °C for 6 h or 1450 °C for 7 days, in good agreement with the XRD patterns of UO_2 (JCPDS card No. 01-075-0421) and $\text{Sm}_2\text{U}_2\text{O}_{8.34}$ (28727-ICSD) in cubic space group $Fm\bar{3}m$, consistent with earlier observations on the formation of Ln_2UO_7 sintered at 1200–1400 °C under neutral or reducing atmospheres [26–33]. However, sintering at higher temperature for longer time (1450 °C for 7 days) can produce better crystalline and homogeneous Dy_2UO_7 in comparison to sintering at 1400 °C for 6 h, refer to the section for microstructures. The refinements of XRD data for both Dy_2UO_7 (Fig. 2a) and Ho_2UO_7 (Fig. 2b) sintered at 1450 °C for 7 days gave good χ^2 values (2.15 for Dy_2UO_7 and 2.30 for Ho_2UO_7) with the refined cell parameters, $a = 5.36749(3)$ Å and $V = 154.637(2)$ Å³ for Dy_2UO_7 , and $a = 5.34976(2)$ Å and $V = 153.110(1)$ Å³ for Ho_2UO_7 . The slight decrease of cell parameters from $a = 5.36749(3)$ Å for Dy_2UO_7 to $a = 5.34976(2)$ Å for Ho_2UO_7 is consistent with the lanthanide ion contraction with an ionic radius in

8-fold coordination of 1.027 Å for Dy^{3+} and 1.015 Å for Ho^{3+} ions.

In general, the phase assemblage will be dependent on two control factors: chemistry and sintering redox conditions. While chemistry control is dominant in some cases such as the formation of NpPO_4 by sintering in air, sintering redox conditions can significantly influence the phase formation of mixed uranium oxides. Sintering in air often results in U partially oxidized to U^{6+} leading to the formation of U_3O_8 as a secondary phase while sintering in Ar- H_2 can stabilize both U^{5+} and U^{4+} in M-U-O systems.

3.2. Microstructures

Apart from the limited structural studies, there is little information on the microstructures of Ln_2UO_7 compounds available in the literature. Consequently, the microstructures for sintered Dy_2UO_7 and Ho_2UO_7 were investigated with both SEM and TEM. The backscattered SEM images (Fig. 3) revealed that the crushed Dy_2UO_7 pellet sintered at 1400 °C for 6 h showed particles in sub-micrometers (Fig. 3a) while the crushed Dy_2UO_7 pellet sintered at 1450 °C for 7 days showed much larger particles in tens of micrometers (Fig. 3b). The EDS multipoint analysis revealed that some areas have higher or lower Dy than U in the sample sintered at 1400 °C for 6 h (Fig. S1), indicating inhomogeneous nature. In contrast, the sample sintered at 1450 °C for 7 days has a more uniform composition with the Dy to U ratio close to unity (Fig. S2). The backscattered SEM images (Fig. 4) for pellets of both Dy_2UO_7 and Ho_2UO_7 sintered at 1450 °C for 7 days showed porous nature with the apparent porosity estimated using the ImageJ software [40] to be ~24 % for Dy_2UO_7 (an example is shown in Fig. S3) and ~10 % for Ho_2UO_7 . The EDS analysis results also confirmed that both samples have nearly ideal stoichiometry as designed (Figs. S4 and S5; Tables S1 and S2). The observed lack of homogeneity in the Dy_2UO_7 sintered at 1400 °C for 6 h may arise from both thermodynamic (temperature) and kinetic (holding time) factors. Subsequently, higher sintering temperature (1450 °C) and longer holding time (7 days) were chosen to address this in order to achieve the successful outcome within a limited time span, which was confirmed by multiple points EDS analyses. The high porosity (~24 %) observed for the Dy_2UO_7 may be related to unsuccessful removal of nitrate from the precursor in the calcination step.

Subsequently, the three samples were further characterized with TEM. For Dy_2UO_7 sintered at 1400 °C for 6 h, the bright field TEM image (Fig. 5a) showed fine particles of Dy_2UO_7 (~5 nm). TEM-EDS analysis results confirmed that the phase contains U, Dy and O with a slightly

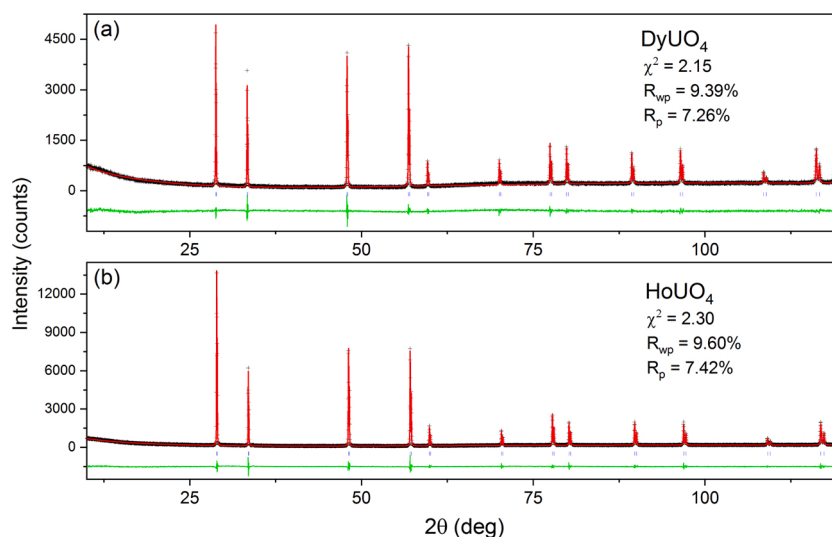


Fig. 2. XRD patterns of samples Dy_2UO_7 (a) and Ho_2UO_7 (b) sintered at 1450 °C in argon with fluorite structures (in cubic space group $Fm\bar{3}m$). Black crosses represent the observed data, and the red line is the fit obtained by the Le Bail method. Blue vertical markers show the peak positions expected in the cubic fluorite structure. The green line underneath records the difference between the observed and the calculated patterns.

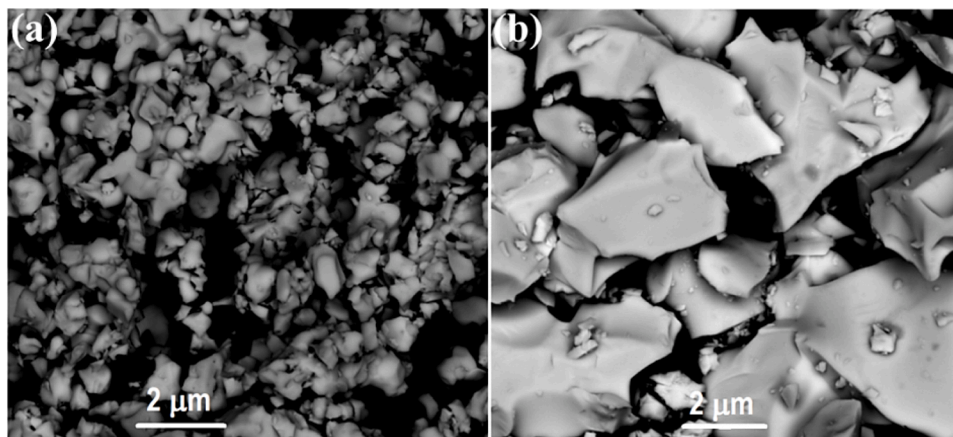


Fig. 3. Backscattered SEM images of crushed sample DyUO₄ either sintered in argon at 1400 °C for 6 h (a) or 1450 °C for 7 days (b).

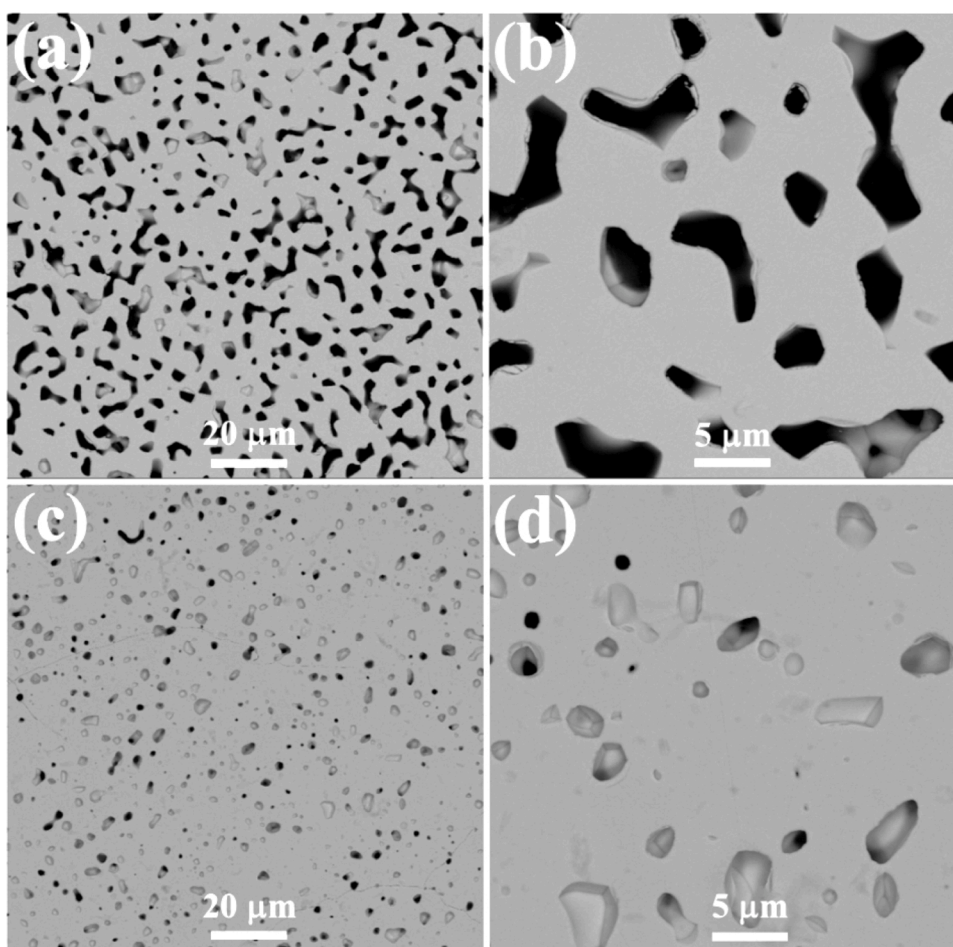


Fig. 4. Backscattered SEM images of sample DyUO₄ [(a) and (b)] and sample HoUO₄ [(c) and (d)] both sintered in argon at 1450 °C for 7 days.

varying atomic ratio of U : Dy, suggesting not quite uniform compositions across the grains (Fig. S6) from the microstructural point of view. The selected area electron diffraction (SAED) pattern in the [051] zone axis as an inset in Fig. 5a was indexed to the cubic fluorite structure. A high resolution TEM (HRTEM) image in the [011] zone axis (Fig. 5b) showed fluorite lattice fringes with a Fast Fourier Transform (FFT) image in the inset. The measured $d(111)$ spacing value is 0.312 nm with the corresponding cell parameter $a = 5.40 \text{ \AA}$. In the case of DyUO₄ sintered at 1450 °C for 7 days, both bright field and dark field TEM images (Fig. 6a and Fig. 6b) showed much larger particles. The HRTEM image

(Fig. 6c) showed typical fluorite lattice fringes with a FFT image in the inset. A SAED pattern in the [011] zone axis (Fig. 6d) was indexed to the cubic fluorite DyUO₄. The measured $d(111)$ spacing value from the HRTEM image (Fig. 6c) is consistent with the cell parameter [$a = 5.36749(3) \text{ \AA}$] refined using the XRD data.

For HoUO₄ sintered at 1450 °C for 7 days, the bright field TEM image (Fig. 7a) showed a large thin section of a crystal. A SAED pattern in the [011] zone axis (Fig. 7b) was indexed to the cubic fluorite HoUO₄ while the HRTEM image in the [011] zone axis (Fig. 7c) with a FFT image as an inset showed the lattice fringes for cubic HoUO₄. The TEM measured

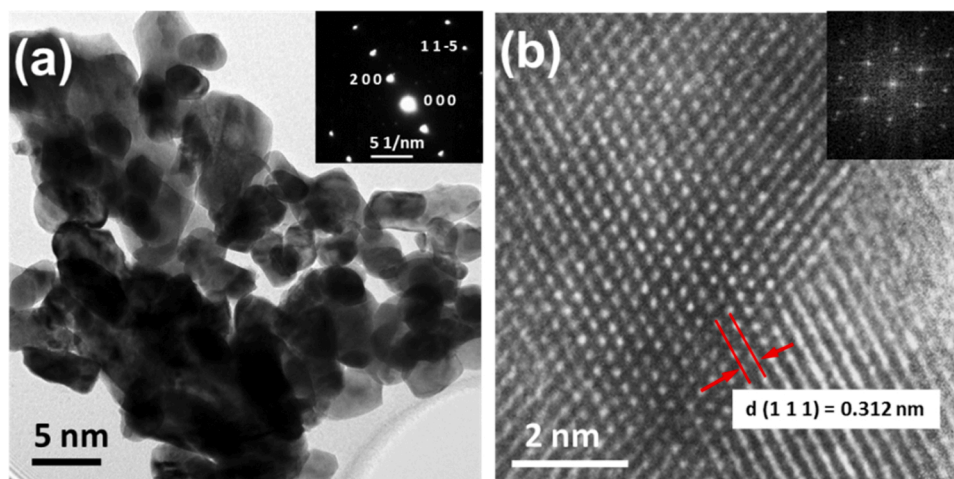


Fig. 5. TEM of the sample DyUO₄ sintered in argon at 1400 °C for 6 h: a bright field image with an inserted SAED pattern indexed in the [051] zone axis (a), a HRTEM image (b) with an inserted FFT image in the [011] zone axis.

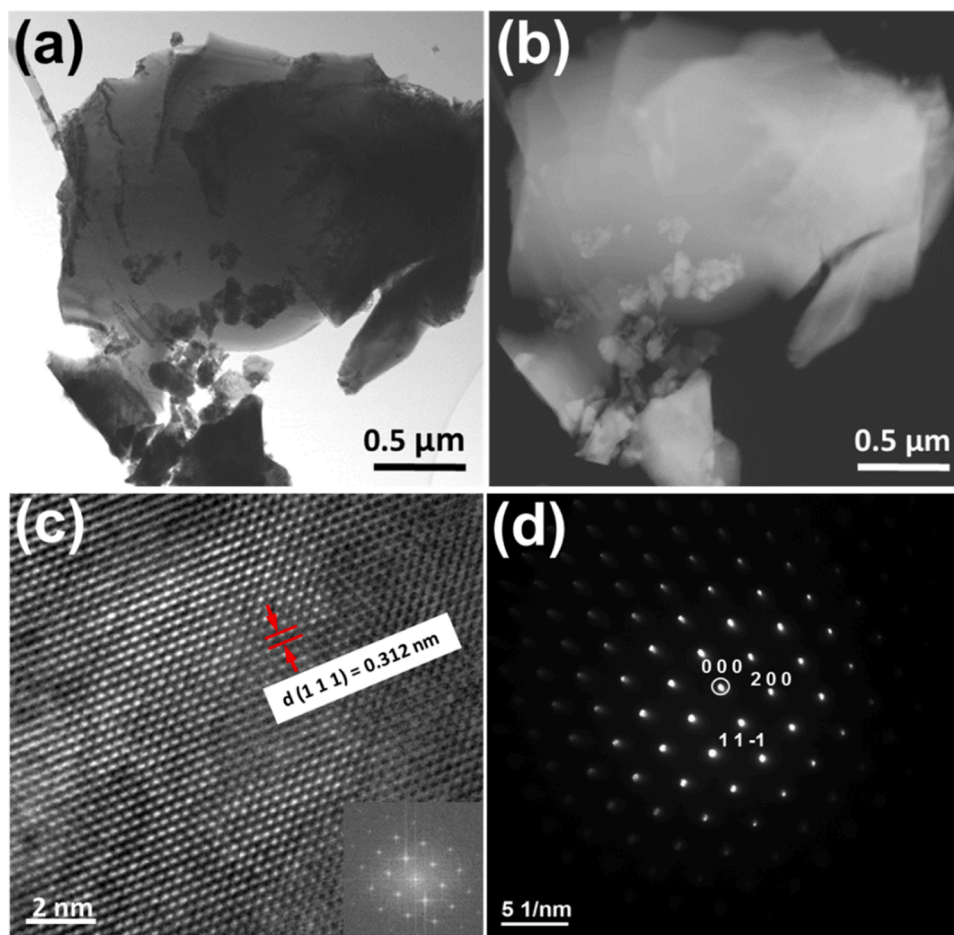


Fig. 6. TEM of the sample DyUO₄ sintered in argon at 1450 °C for 7 days: a bright field (a) and the corresponding dark field (b) TEM images of a crystal, a HRTEM image in the [011] zone axis (c) with an inserted FFT image and an indexed SAED pattern in the [011] zone axis (d).

$d(111)$ spacing value of 0.307 nm is consistent with that determined from the powder XRD.

3.3. Local structures

Raman spectroscopy has been widely used to probe local structural information of various oxides [41–49]. The UO₂ with a cubic structure in

space group $Fm\bar{3}m$ exhibits only one Raman mode as predicted by group theory. This mode corresponds to the symmetric T_{2g} vibration at 445 cm^{-1} . With lanthanide ion incorporations in UO₂, additional Raman modes at higher wavenumbers, $530\text{--}630\text{ cm}^{-1}$, may be observed similar to the situation for α -irradiated UO₂ [50], reflecting the formation of oxygen defects [51,52]. The Raman spectra (Fig. 8) for both DyUO₄ and HoUO₄ sintered at 1450 °C for 7 days showed the typical vibration bands

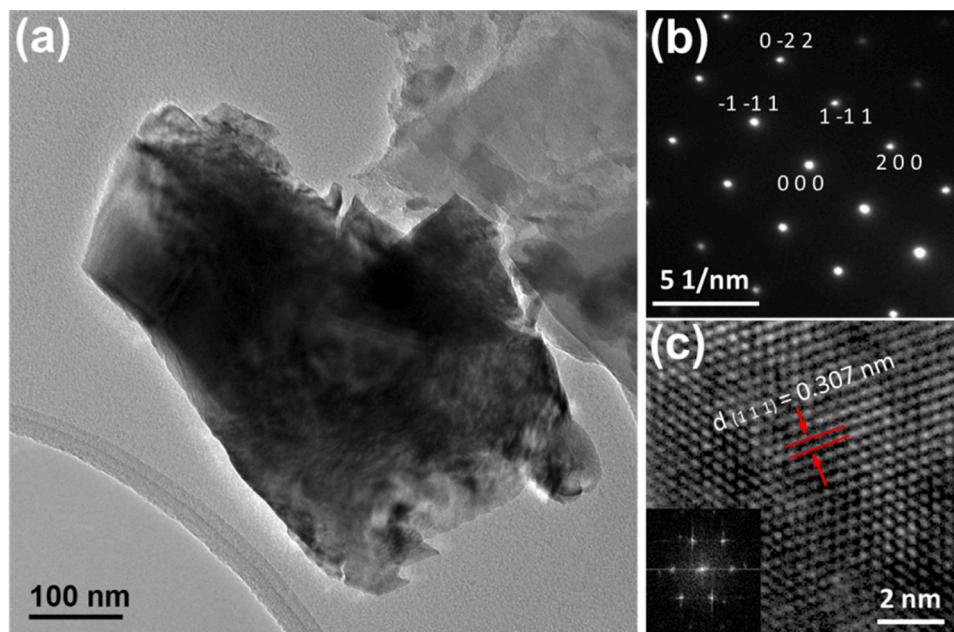


Fig. 7. TEM of the sample HoUO₄ sintered in argon at 1450 °C for 7 days: a bright field TEM image (a); a SAED pattern indexed in the [011] zone axis (b) and a HRTEM image with an inserted FFT image in the [011] zone axis (c).

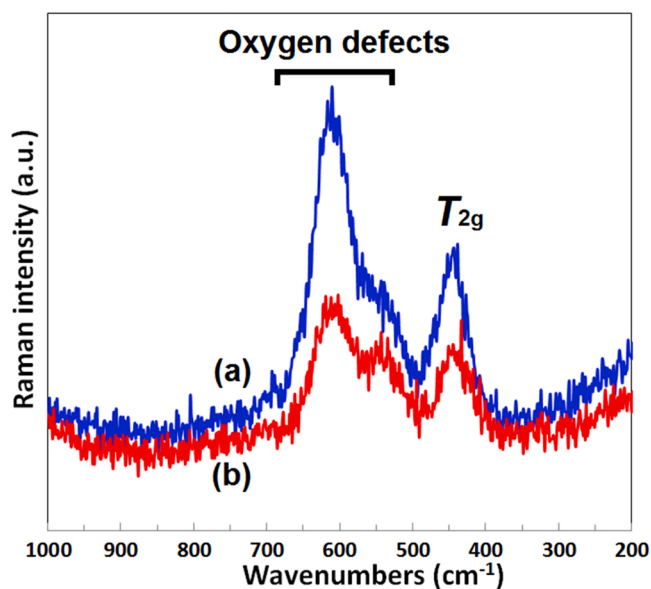


Fig. 8. Raman spectra of samples DyUO₄ (a, blue) and HoUO₄ (b, red) sintered in argon at 1450 °C for 7 days.

expected for the cubic fluorite structure: the T_{2g} mode around 445 cm^{-1} . However, the observed T_{2g} bands broadened and their intensities reduced in comparison to that for pure UO₂ [23], mainly due to the increase of the local cation disorders at the short range distances as a result of the ionic radius difference. In addition, strong new vibration bands appeared at $\sim 530 \text{ cm}^{-1}$ and $\sim 615 \text{ cm}^{-1}$, corresponding to the formation of extensive oxygen defects, e.g., oxygen vacancies. Such strong vibration bands for oxygen defects are uncommon in metal monouranates, reflecting extensive oxygen defects at the short range distances. This may have a profound impact on the physical properties of LnUO₄ materials. In addition, the lack of the U–O stretching mode at $\sim 717 \text{ cm}^{-1}$ infers no formation of UO₈ species with non-bonding oxygens similar to uranyl ions [53,54].

3.4. Uranium valence

Several spectroscopic techniques, e.g., diffuse reflectance spectroscopy (DRS), X-ray photoelectron spectroscopy (XPS) and X-ray absorption near-edge structure (XANES), have been widely used to probe the U valence in oxides [55–59]. The possible U valences in oxides under the experimental conditions are 4+ ($5f^2$ electronic configuration), 5+ ($5f^1$) and 6+ ($5f^0$) states. In DRS, the U⁴⁺ ion gives sharp (zero-phonon line) and broad (vibronic) absorptions across the visible and infrared spectral range [55–58] while the U⁵⁺ ion is confined to the near infrared as it derives only from the crystal-field splitting of ${}^2F_{5/2}$ – ${}^2F_{7/2}$ components (split by spin-orbit coupling) of the 2F electronic state, with the distinguished electronic transitions observable from the splitting of ${}^2F_{7/2}$ at 1538–833 nm (6500–12000 cm^{-1}) range [55–58]. In contrast, the U⁶⁺ ion has no f electrons and the only electronic transitions observable are broad charge-transfer bands in the blue and near-ultraviolet spectral regions.

The DRS spectra of DyUO₄ and HoUO₄ sintered at 1450 °C are shown in Fig. 9. The absorption bands at 1538–833 nm (6500–12,000 cm^{-1}) correspond to a typical $5f^1$ configuration for the U⁵⁺ ion in an octahedral coordination environment [55] while the responsible absorption bands will shift to higher wavelengths for U⁵⁺ ion in an 8-fold coordination environment in a cubic fluorite structure. It is apparent that both DyUO₄ and HoUO₄ contain U⁵⁺ ions evidenced by the presence of weak absorption bands at $\sim 900 \text{ nm}/11111 \text{ cm}^{-1}$ (Fig. 9a) and $\sim 1615 \text{ nm}/6192 \text{ cm}^{-1}$ (Fig. 9b). The absorption bands at $\sim 1615 \text{ nm}$ also suggest that U⁵⁺ ions are on the 8-fold coordination site instead of the 6-fold coordination site such as the U⁵⁺ ion in Dy_{0.5}U_{0.5}Ti₂O₆ brannerite [60], which has the absorption band at $\sim 1445 \text{ nm}/6920 \text{ cm}^{-1}$, relatively lower wavelengths. DRS spectra at the near infrared region (Fig. S7) do not show the sharp absorption bands corresponding to U⁴⁺ ion, clearly indicating the absence of U⁴⁺ ions in both compounds. To further confirm these findings, XPS was also used to study the U valence in HoUO₄.

Because XPS is an extremely surface sensitive technique, it is crucial to first remove the oxidized surface layer so that the results are representative of the bulk. This was achieved by examining a freshly polished HoUO₄ sample. Note that the DyUO₄ sample was not analyzed using XPS due to its higher porosity. The U 4f XPS spectrum of HoUO₄ is shown in Fig. 10, displaying two main photoemission lines (U4f_{7/2} and U4f_{5/2})

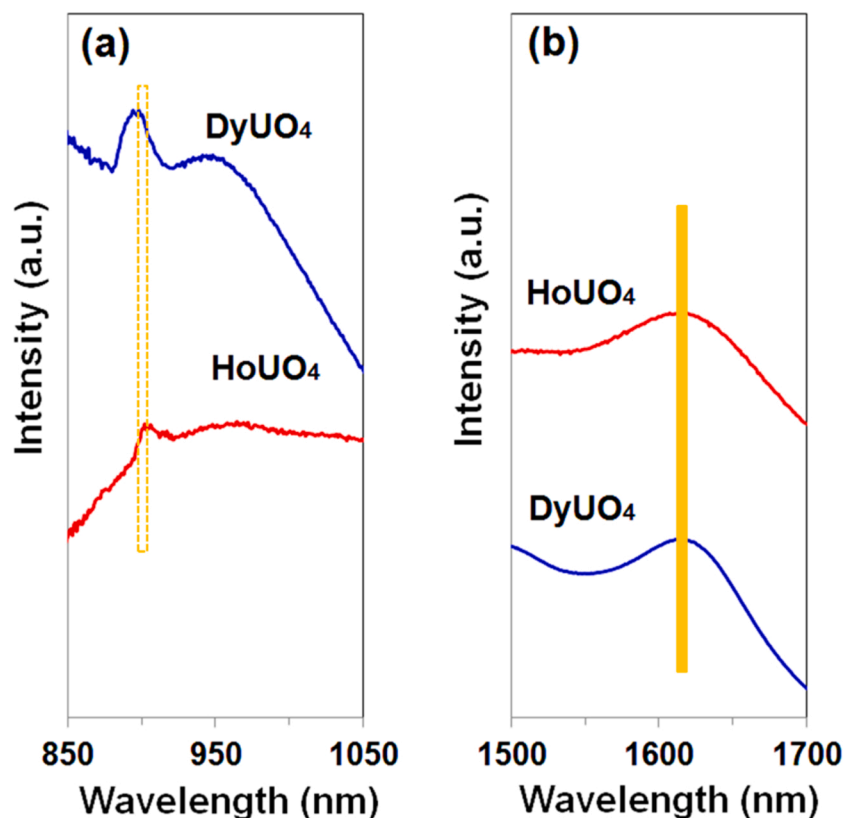


Fig. 9. Diffuse reflectance spectra in 850–1050 nm region (a) and 1500–1700 nm region (b) of samples DyUO₄ (blue) and HoUO₄ (red) sintered in argon at 1450 °C for 7 days.

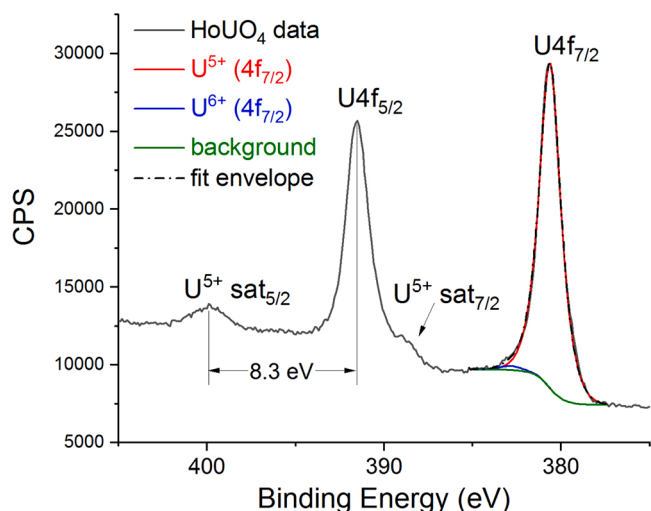


Fig. 10. XPS spectrum of the U 4f region for sample HoUO₄ sintered in argon at 1450 °C for 7 days.

around 10.9 eV apart due to spin-orbit splitting along with their corresponding satellite peaks. It is well known that the U 4f binding energy (BE) and the energy difference between the satellite and corresponding primary U 4f peak (ΔE_{s-p}) are very sensitive to the U oxidation state [61, 62]. As shown in Fig. 10, the U4f_{7/2} line was fitted with two mixed Gaussian/Lorentzian peaks after subtracting a Shirley-type background. The peak position and width were allowed to vary freely, but the width of the two peaks was constrained to be equal. The strong peak (~99 %) is located at 380.6 eV, in excellent agreement with NaU⁵⁺O₃ [63]. The very weak peak (~1 %) at 382.8 eV is attributed to surface oxidation due

to the sample being exposed to air briefly [5562]. In addition to monitoring the BE of the U 4f peaks, the satellite structure provides even more definitive signature of the U valence, because not only ΔE_{s-p} is sensitive to the U oxidation state but also the number of satellite peaks and their relative intensity to the main peak [64]. Pentavalent uranium in ternary uranium oxides is known to have a single satellite peak with $\Delta E_{s-p} \sim 7.8$ –8.3 eV, while hexavalent and tetravalent uranium oxides display two satellite peaks at about 4 and 10 eV (U⁶⁺) and one satellite peak at ~6.9 eV (U⁴⁺), respectively [61, 64]. Fig. 10 clearly shows a single satellite peak at 8.3 eV above the U U4f_{5/2} peak, confirming that the HoUO₄ sample contains U⁵⁺ only (note that the position of the U4f_{7/2} satellite cannot be determined accurately due to the overlap with the U4f_{5/2} peak). Overall, both DRS and XPS investigations confirmed that DyUO₄ and HoUO₄ sintered in argon at 1450 °C are pure pentavalent monouranates.

3.5. Magnetic properties

In the literature, limited magnetic property investigations are available for MUO₄ phases with trivalent M ions. The magnetic susceptibility measurements for BiUO₄, ScUO₄ and YUO₄ confirmed that they are pentavalent monouranates [24, 25]. They showed the same maximum at 4–7 K with a similar shape in the magnetic susceptibility vs. temperature curves, with the effective magnetic moment consistent with $S = 1/2$, implying the U⁵⁺ state. For LnUO₄ pentavalent monouranates, it was anticipated that magnetic interactions may involve coupling of the U⁵⁺ and (Dy/Ho)³⁺ ions. Surprisingly, both DyUO₄ and HoUO₄ showed typical paramagnetic behaviour down to ~2 K with no obvious long range magnetic orders (Fig. 11). This could arise from the extensive oxygen defects or cation disorders on a single fluorite metal site or both. However, the exact reason for the observed result needs further experimental evidence and deserve a future investigation, ideally a neutron diffraction study, which requires synthesis of a

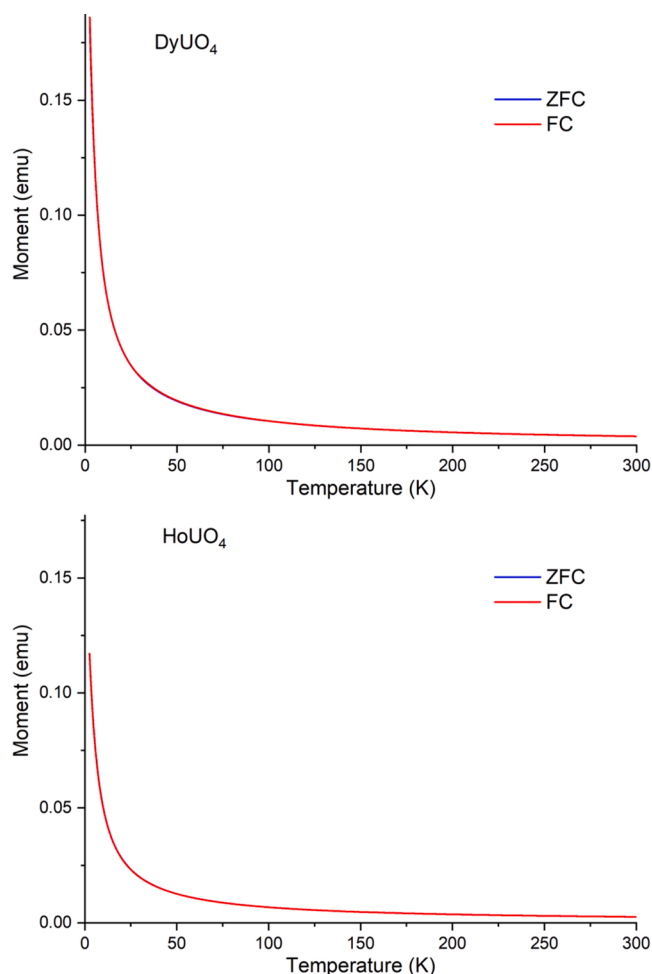


Fig. 11. Magnetic susceptibility measurements of Dy_2UO_7 (a) and Ho_2UO_7 (b) sintered in argon at 1450 °C for 7 days. Note that the ZFC and FC data overlap with each other.

gram-scale sample.

3.6. Further discussion and implications

With the incorporation of trivalent cations in UO_2 , it is generally accepted that trivalent cations are located on the uranium site in the solid solution. Such an assumption is often supported by the cell parameter modelling with a Vegard's law over a range of compositions, if the cubic fluorite structure remains after doping [65]. However, some metal uranates have different crystal structures. For example, both CrUO_4 and FeUO_4 have orthorhombic structure in space group $Pbcn$ [18–20], with Cr^{3+} and Fe^{3+} cations in six coordination polyhedra instead of cubic ones. Consequently, a collective re-arrangement of Cr^{3+} cations and oxygen anions was proposed [50,52]. For trivalent cations suitable for an eight-fold coordination environment in cubic structures such as $(\text{Bi}/\text{Sc}/\text{Y})^{3+}$ and Ln^{3+} cations [66], their direct substitutions on the uranium site are anticipated.

The evolution of the unit-cell volumes of LnUO_4 and related $\text{M}^{\text{III}}\text{UO}_4$ ($\text{M} = \text{Sc}, \text{Y}$ and Bi) phases as a function of the ionic radius for the eight-fold coordination geometry (Fig. 12, Table S3) can be described well by a linear relationship, reflecting the general trend for ionic radius contraction along the lanthanide series. As pentavalent oxidation state of uranium was proven for $\text{M}^{\text{III}}\text{UO}_4$ ($\text{M}^{\text{III}} = \text{Bi}, \text{Sc}$, and Y) based on magnetic susceptibility measurements [24,25], it is anticipated that all the LnUO_4 compositions are indeed pure pentavalent monouranates, consistent with the uranium valence investigations in this work.

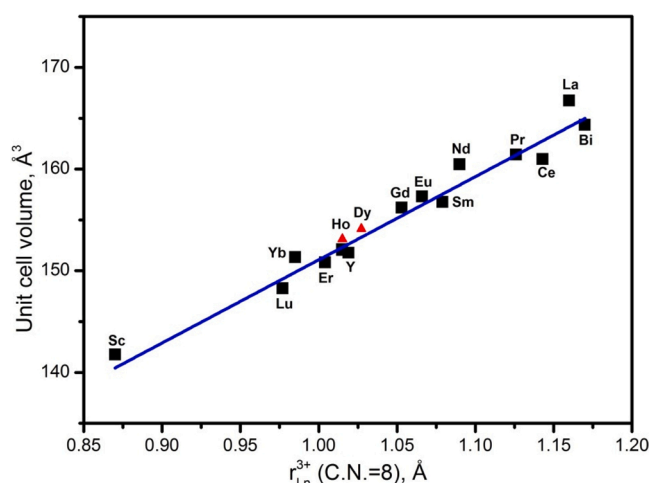


Fig. 12. Cell volumes (Å^3) versus ionic radii of cations in 8-fold coordination geometry for $\text{M}^{\text{III}}\text{UO}_4$ ($\text{M} = \text{Bi}, \text{Sc}$ and Y) and LnUO_4 (Table S3) in space group $Fm\bar{3}m$, with the data points obtained in this study marked as red triangles.

4. Conclusions

Uranium ternary oxides with lanthanide ions are fundamentally important owing to their potential applications as accident tolerance fuels and possible waste forms for spent nuclear fuels. The aim of this work was to investigate LnUO_4 ($\text{Ln} = \text{Dy}$ and Ho), in specific the phase formation, structures and microstructures, uranium valence and magnetic properties. Although sintering in argon at 1400 °C for 6 h can produce pure solid solution of LnUO_4 , microstructural studies uncovered that sintering at higher temperature for longer time (1450 °C for 7 days) favours the formation of better crystallinity with improved homogeneity. Both DyUO_4 and HoUO_4 are cubic structured pentavalent uranium ternary oxides with their structures refined using X-ray diffraction data in space group $Fm\bar{3}m$, and supported with both transmission electron microscopy and Raman spectroscopy. The presence of pure pentavalent uranium in these two oxides was verified using a combination of diffuse reflectance and X-ray photoelectron spectroscopies. Surprisingly, the magnetic susceptibility measurements revealed that both DyUO_4 and HoUO_4 are paramagnetic showing no long-range magnetic orders, which is most likely due to the extensive local oxygen defects and Ln/U disorder over the single metal site in the fluorite-type structure, supported by Raman spectroscopy. However, the hypothesis needs to be further investigated and verified with a future potential neutron diffraction study.

Declaration of Competing Interest

The authors report no declarations of interest.

Acknowledgements

The authors wish to thank Dr. I. Karatchevtseva for Raman measurements, Dr. O. Muransky for porosity estimations, and Nuclear Science and Technology Landmark Infrastructure (NSTLI) at ANSTO for synthesis and characterization of materials. The XPS measurements were carried out at the Surface Analysis Laboratory of the University of New South Wales, Sydney.

Appendix A. Supplementary data

Supplementary material related to this article can be found, in the online version, at doi:<https://doi.org/10.1016/j.jeurceramsoc.2021.05.040>.

References

- [1] H.R. Hoekstra, R.H. Marshall, Some uranium-transition element double oxides, *Adv. Chem. Ser.* (1967) 211–227.
- [2] P.A.G. Ohare, J. Boerio, H.R. Hoekstra, Thermochemistry of uranium compounds VIII. Standard enthalpies of formation at 298.15 K of the uranates of calcium (CaUO_4) and barium (BaUO_4). Thermodynamics of the behavior of barium in nuclear fuels, *J. Chem. Thermodyn.* 8 (1976) 845–855.
- [3] G.L. Murphy, Z. Zhang, B.J. Kennedy, The solid-state chemistry of AUO_4 ternary uranium oxides: a review, in: T. Vogt, D. Burtrey (Eds.), *Complex Oxides*, World Scientific, 2019.
- [4] M. Bühl, R. Diss, G. Wipff, Coordination environment of aqueous uranyl(VI) ion, *J. Am. Chem. Soc.* 127 (39) (2005) 13506–13507.
- [5] J. Yeon, M.D. Smith, J. Tapp, A. Möller, H.-C. zur Loye, Application of a mild hydrothermal approach containing an in situ reduction step to the growth of single crystals of the quaternary U(IV)-containing fluorides $\text{Na}_4\text{MU}_6\text{F}_{30}$ ($\text{M} = \text{Mn}^{2+}$, Co^{2+} , Ni^{2+} , Cu^{2+} , and Zn^{2+}) crystal growth, structures, and magnetic properties, *J. Am. Chem. Soc.* 136 (2014) 3955–3963.
- [6] P.C. Burns, R.C. Ewing, F.C. Hawthorne, The crystal chemistry of hexavalent uranium; polyhedron geometries, bond-valence parameters, and polymerization of polyhedra, *Canad. Mineral.* 35 (1997) 1551–1570.
- [7] R.J. Baker, Uranium minerals and their relevance to long term storage of nuclear fuels, *Coord. Chem. Rev.* 266–267 (2014) 123–136.
- [8] P.C. Burns, U^{6+} minerals and inorganic compounds: insights into an expanded structural hierarchy of crystal structures, *Canad. Mineral.* 43 (2005) 1839–1894.
- [9] A. Lussier, J.R.A.K. Lopez, P.C. Burns, A revised and expanded structure hierarchy of natural and synthetic hexavalent uranium compounds, *Canad. Mineral.* 54 (2016) 177–283.
- [10] J. Selbin, J.D. Ortego, Chemistry of uranium(V), *Chem. Rev.* 69 (1969) 657–671.
- [11] A. Navrotsky, T. Shvareva, X. Guo (Eds.), *Thermodynamics of Uranium Minerals and Related Materials*, Mineralogical Association of Canada, 2013, pp. 147–164, chapter 4.
- [12] K.A. Kraus, F. Nelson, Chemistry of aqueous uranium(V) solutions. II. Reaction of uranium pentachloride with water. Thermodynamic stability of UO_2^{2+} . Potential of U(IV)/(V), U(IV)/(VI) and U(V)/(VI) couples, *J. Am. Chem. Soc.* 71 (1949) 2517–2522.
- [13] D. Cohen, The preparation and spectrum of uranium(V) ions in aqueous solutions, *J. Inorg. Nucl. Chem.* 32 (1970) 3525–3530.
- [14] G.L. Murphy, B.J. Kennedy, B. Johannessen, J.A. Kimpton, M. Avdeev, C.S. Griffith, G.J. Thorogood, Z.M. Zhang, Structural studies of the rhombohedral and orthorhombic monouranates: CaUO_4 , $\alpha\text{-SrUO}_4$, $\beta\text{-SrUO}_4$ and BaUO_4 , *J. Solid State Chem.* 237 (2016) 86–92.
- [15] G.L. Murphy, B.J. Kennedy, J.A. Kimpton, Q.F. Gu, B. Johannessen, G. Beridze, P. M. Kowalski, D. Bosbach, M. Avdeev, Z.M. Zhang, Nonstoichiometry in strontium uranium oxide: Understanding the rhombohedral—Orthorhombic transition in SrUO_4 , *Inorg. Chem.* 55 (2016) 9329–9334.
- [16] G.L. Murphy, C. Wang, G. Beridze, Z. Zhang, J.A. Kimpton, M. Avdeev, P. M. Kowalski, B.J. Kennedy, An unexpected crystallographic phase transformation in non-stoichiometric SrUO_{4-x} : reversible oxygen defect ordering and symmetry lowering with increasing temperature, *Inorg. Chem.* 57 (2018) 5948–5958.
- [17] G.L. Murphy, P. Kegler, Y. Zhang, Z. Zhang, E.V. Alekseev, M. Daly de Jonge, B. J. Kennedy, High pressure synthesis, structural and spectroscopic studies of the Ni-U-O system, *Inorg. Chem.* 57 (21) (2018) 13847–13858.
- [18] G.L. Murphy, Z. Zhang, R. Tesch, P.M. Kowalski, M. Avdeev, E.Y. Kuo, D.J. Gregg, P. Kegler, E.V. Alekseev, B.J. Kennedy, Tilting and distortion in rutile-related mixed metal ternary uranium oxides: a structural, spectroscopic, and theoretical investigation, *Inorg. Chem.* 60 (2021) 2246–2260.
- [19] C.M. Read, M.D. Smith, H.-C. zur Loye, Single crystal growth and structural characterization of ternary transition-metal uranium oxides: MnUO_4 , FeUO_4 , and NiU_2O_6 , *Solid State Sci.* 37 (2014) 136–143.
- [20] X. Guo, E. Tiferet, L. Qi, J.M. Solomon, A. Lanzirrotti, M. Newville, M.H. Engelhard, R.K. Kukkadapu, D. Wu, E.S. Ilton, M. Asta, S.R. Sutton, H. Xua, A. Navrotsky, U(V) in metal uranates: a combined experimental and theoretical study of MgUO_4 , CrUO_4 , and FeUO_4 , *Dalton Trans.* 45 (2016) 4622–4632.
- [21] S. Sampath, A. Chadha, D.M. Chackraburmy, Thermal behaviour of co-precipitated mixtures of chromium(III) and uranium(VI), *Thermochimica Acta* 55 (2) (1982) 249–251.
- [22] M.W.D. Cooper, D.J. Gregg, Y. Zhang, G.J. Thorogood, G.R. Lumpkin, R.W. Grimes, S.C. Middleburgh, Formation of $(\text{Cr,Al})\text{UO}_4$ from doped UO_2 and its influence on partition of soluble fission products, *J. Nucl. Mater.* 443 (2013) 236–241.
- [23] K. Popa, D. Prieur, D. Manara, M. Naji, J.-F. Vigier, P.M. Martin, O. Dieste Blanco, A.C. Scheinost, T. Prüjmann, T. Vitova, P.E. Raison, J. Somersa, R.J.M. Konings, Further insights into the chemistry of the Bi-U-O system, *Dalton Trans.* 45 (2016) 7847–7855.
- [24] C. Miyake, T. Isobe, Y. Yoneda, S. Imoto, Magnetic properties of pentavalent uranium ternary oxides with fluorite structure: ScUO_4 , YUO_4 , CaU_2O_6 and CdU_2O_6 , *Inorg. Chim. Acta* 140 (1987) 137–140.
- [25] C. Miyake, O. Kawasaki, K. Gotoh, A. Nakatani, Magnetic properties of pentavalent uranium fluorite structure Part II, *J. Alloys Compd* 200 (1993) 187–190.
- [26] F. Hund, U. Peetz, Z. Anorg. Allg. Chem. 267 (1952) 189–197.
- [27] F. Hund, U. Peetz, Z. Anorg. Allg. Chem. 271 (1952) 6–16.
- [28] F. Hund, U. Peetz, G. Kottenhahn, Z. Anorg. Allg. Chem. 278 (1955) 184–191.
- [29] W. Rüdorff, S. Kemmler, H. Leutner, Ternäre Uran(V)-oxyde [1], *Angew. Chem.* 12 (1962) 429.
- [30] J. Selbin, J.D. Ortego, Chemistry of uranium (V), *Chem. Rev.* 69 (1968) 657–671.
- [31] H. Weitzel, C. Keller, Neutron diffraction studies of $(\text{RE}_{0.5}\text{U}_{0.5})\text{O}_2$ ($\text{RE} = \text{Y, La, Nd, Ho, and Lu}$), *J. Solid State Chem.* 13 (1975) 136–141.
- [32] I.B. de Alleluia, M. Hoshi, W.G. Jocher, C. Keller, Phase relationships for the ternary $\text{UO}_2\text{-UO}_2\text{-REO}_{1.5}$ ($\text{RE} = \text{Pr, Nd, Dy}$) systems, *J. Inorg. Nucl. Chem.* 43 (1981) 1831–1834.
- [33] Y. Hinatsu, T. Fujino, Studies on magnetic properties of $\text{UO}_2\text{-CeO}_2$ solid solutions III: magnetic susceptibilities of solid solutions with high cerium concentrations, *J. Less-Common Met.* 149 (1989) 197–205.
- [34] B. Herrero, R. Bès, F. Audubert, N. Clavier, M.O.J.Y. Hunault, G. Baldinozzi, Charge compensation mechanisms in Nd-doped UO_2 samples for stoichiometric and hypo-stoichiometric conditions: lack of miscibility gap, *J. Nucl. Mater.* 539 (2020), 152276.
- [35] R. Bès, K. Kvashnina, A. Rossberg, G. Dottavio, L. Desgranges, Y. Pontillon, P. L. Solari, S.M. Butorin, P. Martin, New insight in the uranium valence state determination in $\text{U}_y\text{Nd}_{1-y}\text{O}_{2+x}$, *J. Nucl. Mater.* 507 (2018) 145–150.
- [36] R. Bès, J. Pakarinen, A. Baena, S. Conradson, M. Verwerf, F. Tuomisto, Charge compensation mechanisms in $\text{U}_{1-x}\text{Gd}_x\text{O}_2$ and $\text{Th}_{1-x}\text{Gd}_x\text{O}_{2+x/2}$ studied by X-ray absorption spectroscopy, *J. Nucl. Mater.* 489 (2017) 9–21.
- [37] A. Le Bail, H. Duroy, J.L. Fourquet, Ab-initio structure determination of LiSbWO_6 by X-ray powder diffraction, *Mater. Res. Bull.* 23 (1988) 447–452.
- [38] B.A. Hunter, Rietica – a visual rietveld program, *Int. Union Crystallogr. Commis. Powder Diffr. Newslett.* 20 (1998) 21.
- [39] N. Fairley, CasaXPS Version 2.3.23PR1.0, Casa Software Ltd., Teignmouth, UK, 2020.
- [40] W. Rasband, ImageJ 1.52d, National Institutes of Health, USA.
- [41] T. Shimanouchi, M. Tsuboi, T. Miyazawa, Optically active lattice vibrations as treated by the GF-matrix method, *J. Chem. Phys.* 35 (1961) 1597–1612.
- [42] V.G. Keramidis, W.B. White, Raman spectra of oxides with the fluorite structure, *J. Chem. Phys.* 59 (1973) 1561–1562.
- [43] D. Manara, B. Renker, Raman spectra of stoichiometric and hyperstoichiometric uranium dioxide, *J. Nucl. Mater.* 321 (2003) 233–237.
- [44] T. Livneh, E. Sterer, Effect of pressure on the resonant multiphonon Raman scattering in UO_2 , *Phys. Rev. B: Condens. Matter* 73 (2006), 085118.
- [45] C. Jégou, R. Caraballo, S. Peugot, D. Roudil, L. Desgranges, M. Magnin, Raman spectroscopy characterization of actinide oxides ($\text{U}_{1-y}\text{Pu}_y\text{O}_2$): resistance to oxidation by the laser beam and examination of defects, *J. Nucl. Mater.* 405 (2010) 235–243.
- [46] M.J. Sarsfield, R.J. Taylor, C. Puxley, H.M. Steele, Raman spectroscopy of plutonium dioxide and related materials, *J. Nucl. Mater.* 427 (2012) 333–342.
- [47] R. Böhrer, M.J. Welland, D. Prieur, P. Cakir, T. Vitova, T. Pruessmann, I. Pidchenko, C. Hennig, C. Guéneau, R.J.M. Konings, D. Manara, Recent advances in the study of the $\text{UO}_2\text{-PuO}_2$ phase diagram at high temperatures, *J. Nucl. Mater.* 448 (2014) 330–339.
- [48] L. Medyk, D. Manara, J.-Y. Colle, D. Bouexière, J.F. Vigier, L. Marchetti, P. Simon, P.h. Martina, Determination of the plutonium content and O/M ratio of $(\text{U,Pu})\text{O}_{2-x}$ using Raman spectroscopy, *J. Nucl. Mater.* 541 (2020), 152439.
- [49] D. Horlait, L. Claparède, N. Clavier, S. Szenknecht, N. Dacheux, J. Ravaut, R. Podor, Stability and structural evolution of $\text{Ce}_{1-x}\text{Ln}_x\text{O}_{2+x/2}$ solid solutions: a coupled $\mu\text{-Raman/XRD}$ approach, *Inorg. Chem.* 50 (2011) 7150–7161.
- [50] L. Desgranges, G. Guimbretière, P. Simon, F. Duval, A. Canizares, R. Omnee, C. Jegou, R. Caraballo, Annealing of the defects observed by Raman spectroscopy in UO_2 irradiated by 25 MeV He^{2+} ions, *Nucl. Inst. Methods B* 327 (2014) 74–77.
- [51] L. Desgranges, G. Baldinozzi, P. Simon, G. Guimbretière, A. Canizares, Raman spectrum of U_4O_9 : a new interpretation of damage lines in UO_2 , *J. Raman Spectrosc.* 43 (2012) 455–458.
- [52] L. Desgranges, P. Simon, P.H. Martin, G. Guimbretière, G. Baldinozzi, What can we learn from Raman spectroscopy on irradiation-induced defects in UO_2 ? *JOM* 66 (12) (2014) 2546–2552.
- [53] M.L. Palacios, S.H. Taylor, Characterization of uranium oxides using *in situ* micro-Raman spectroscopy, *Appl. Spectrosc.* 54 (2000) 1372–1378.
- [54] F. Pointurier, O. Marie, Identification of the chemical forms of uranium compounds in micrometer-size particles by means of micro-Raman spectrometry and scanning electron microscope, *Spectrochim. Acta, Part B* 65 (2010) 797–804.
- [55] K.S. Finnie, Z. Zhang, E.R. Vance, M.L. Carter, Examination of U valence states in the brannerite structure by near-infrared diffuse reflectance and X-ray photoelectron spectroscopies, *J. Nucl. Mater.* 317 (2003) 46–53.
- [56] E.R. Vance, Y. Zhang, Diffuse reflectance spectra of U ions in ThO_2 , *J. Nucl. Mater.* 357 (2006) 77–81.
- [57] E.R. Vance, Y. Zhang, T. McLeod, J. Davis, Actinide valences in xenotime and monazite, *J. Nucl. Mater.* 409 (2011) 221–224.
- [58] E.R. Vance, Y. Zhang, Z. Zhang, Diffuse reflectance and X-ray photoelectron spectroscopy of uranium in ZrO_2 and $\text{Y}_2\text{Ti}_2\text{O}_7$, *J. Nucl. Mater.* 400 (2010) 8–14.
- [59] D.J. Gregg, Z.M. Zhang, G.J. Thorogood, B.J. Kennedy, J.A. Kimpton, G.J. Griffiths, P.R. Guagliardo, G.R. Lumpkin, E.R. Vance, Cation antisite disorder in uranium-doped gadolinium zirconate pyrochlores, *J. Nucl. Mater.* 452 (1–3) (2014) 474–478.
- [60] Y. Zhang, T. Wei, Z. Zhang, L. Kong, P. Dayal, D.J. Gregg, Uranium brannerite with Tb(III)/Dy(III) ions: phase formation, structures, and crystallizations in glass, *J. Am. Ceram. Soc.* 102 (12) (2019) 7699–7709.
- [61] E.S. Ilton, P.S. Bagus, XPS determination of uranium oxidation states, *Surf. Interface Anal.* 43 (13) (2011) 1549–1560.
- [62] M. Colella, G.R. Lumpkin, Z. Zhang, E.C. Buck, K.L. Smith, Determination of the uranium valence state in the brannerite structure using EELS, XPS, and EDX, *Phys. Chem. Miner.* 32 (1) (2005) 52–64.

- [63] J.H. Liu, S. Van den Berghe, M.J. Konstantinovic, XPS spectra of the U^{5+} compounds KUO_3 , $NaUO_3$ and $Ba_2U_2O_7$, *J. Solid State Chem.* 182 (5) (2009) 1105–1108.
- [64] T. Gouder, R. Eloirdi, R. Caciuffo, Direct observation of pure pentavalent uranium in U_2O_5 thin films by high resolution photoemission spectroscopy, *Sci. Rep.* 8 (1) (2018) 8306.
- [65] T. Ohmichi, S. Fukushima, A. Maeda, H. Watanabe, On the relation between lattice parameter and O/M ratio for uranium dioxide – trivalent rare earth oxide solid solution, *J. Nucl. Mater.* 102 (1981) 40–46.
- [66] Z. Talip, T. Wiss, P.E. Raison, J. Paillier, D. Manara, J. Somers, R.J.M. Konings, Raman and X-ray studies of uranium–lanthanum-mixed oxides before and after air oxidation, *J. Am. Ceram. Soc.* 98 (7) (2015) 2278–2285.